Research Article

TRR
JOURNAL OF THE TRANSPORTATION RESEARCH BOARD

Transportation Research Record
2021, Vol. 2675(8) 603–612

DOI: 10.1177/03611981211999605
journals.sagepub.com/home/trr
SAGE

Grayscale Drone Inspection Image Enhancement Framework for Advanced Bridge Defect Measurement

Euiseok Jeong[1], Junwon Seo[1], and James Wacker[2]

Abstract

This paper presents a framework to better identify and measure defects in a bridge using drone-based inspection images integrated with grayscale image enhancement techniques. For this study, a DJI Matrice 210 drone was used for the inspection of a three-span timber bridge with concrete decking located in Keystone, South Dakota. During the inspection, the drone recorded a series of videos of the bridge using the MOVie (MOV, video file extension) video format. MOV-based image analysis was conducted to identify a variety of defect types (i.e., efflorescence, water leakage, spalling, and discoloration) on the bridge. For improvement of defect visibility, the grayscale image enhancement technique was applied to determine visually enhanced images for the individual defect. The technique used grayscale image histogram processing that can adjust images using realignment of contrast histograms, in which contrasts of each pixel of the grayscale images have their own number from 0 for black to 255 for white in the image. With the enhanced images, pixel-based measurement was conducted to quantify the defects, including efflorescence ($3.75\,m^2$), water leakage ($4.21\,m^2$), spalling ($0.74\,m^2$), and discoloration ($2.12\,m^2$). Based on these findings, the grayscale drone inspection image enhancement technique enabled the demonstration of defect visibility adjustment and improvement for more reliable identification and measurement of the defects in the bridge.

Periodic bridge inspection is one of the most important tasks to ensure bridges are safe and remain in sound condition. Inspectors and engineers have conducted visual inspections and defect quantifications using conventional inspection tools such as digital cameras, measuring tapes, and so on. To complete bridge inspections using the conventional tools, inspectors may access the defected area on the bridge with specialized vehicles such as under bridge inspection vehicles/trucks (UBIVs/UBITs) if the critical defect is in hard-to-access areas. However, this was not found to be an effective approach as it requires traffic closures or control for the safety of inspectors. The use of rope access, which allows to eliminate the need for traffic control, can be considered an alternative to perform bridge inspections, but a high proficiency with all safety equipment is required to inspect the bridges safely and efficiently. Most importantly, the safety of rope access inspectors is uncertain (*1*). To resolve these issues, bridge inspections using drones have been frequently adopted by many researchers (*2–14*). Particularly, drones can provide easier accessibility and straightforward maneuverability to the inspectors to record a high volume of videos and images for visual defect detection of a bridge.

Although the drone-enabled inspection is a useful approach to identify the defects, the inherent limitation of the image analysis may impede the accurate quantification of the defects because of inaccurate and insufficient defect boundary information. Many studies have suggested various image processing techniques including pixel-based measurement (*15*), pattern recognition (*16–18*), and digital image correlation (*7, 19–21*). Especially, defect measurement using the pixel-based measurement technique (*15*) is regarded as a commonly used suitable technique to quantify specific defects such as spalling, efflorescence, and discoloration. For example, the spalling length can be measured from the number of pixels present in the defect on the image, which is the relative length based on the counted pixels. To obtain the actual length, the reference length that is the length of one of the bridge elements (e.g., girder width) is

[1]Department of Civil and Environmental Engineering, South Dakota State University, Brookings, SD
[2]United States Department of Agriculture-Forest Service, Forest Products Laboratory, Madison, WI

Corresponding Author:
Junwon Seo, Junwon.Seo@sdstate.edu

required from which the actual length can be calculated with the ratio of the number of pixels between the reference and relative lengths of the defects. However, to calculate the area of such spalling accurately, this technique may face challenges for detecting the clear boundaries of defects.

To improve the accuracy of the pixel-based measurement, high-quality inspection images are required. Some bridge inspection images obtained from drones may have low quality because of poor exposure conditions. For instance, it is challenging to detect defects on low-quality images because of low brightness or over-exposure. These issues can hamper feasible defect quantification using drone inspection images. To resolve these issues, various types of image enhancement processing (*22*) were suggested such as thresholding transformation, intensity transformation, logarithmic transformation, power-law transformation, and grayscale image histogram processing (*23*). Among these techniques, the grayscale image histogram processing can adjust images using realignment of contrast histograms, in which contrasts for each pixel of the grayscale images have their own number from 0 to 255 in the image. There is no literature that reports these techniques being applied to timber bridge superstructures.

This paper is aimed at performing the bridge defect identification and measurement through grayscale drone inspection image enhancement techniques using a timber girder bridge. This paper consists of six sections including this introduction. The following section explains a proposed framework for advanced drone-based bridge inspection and defect quantification using the grayscale image enhancement techniques. The third and fourth sections, respectively, present the bridge selected in this study and a description of the selected drone. The fifth section details the results and discussion on the defect measurement. The final section discusses the principal conclusions derived from this study.

Framework

This framework consists of two steps: (a) bridge inspection and (b) image processing as shown in Figure 1. In the first step, a bridge inspection is performed using a drone. Before the drone-enabled inspection, weather checking, bridge owner permission, battery check, airspace authorization, pre-flight checklist of the Federal Aviation Administration (*24*), and firmware update for the drone and remote controller are performed. Weather checking is one of the most important tasks during inspection preparation as drones cannot be controlled efficiently when wind speed exceeds 13 m/s. During the inspection, the drone observes and records several videos (MOV extension) for image acquisition without any omission errors. Video recording can be considered a suitable image-capturing method capable of extracting several high-quality inspection images (i.e., 25 images per second). The remote pilot shall identify the defects and measure, as a minimum, a dimension of one of the structural elements that should be utilized as a reference length during the pixel-based defect quantification.

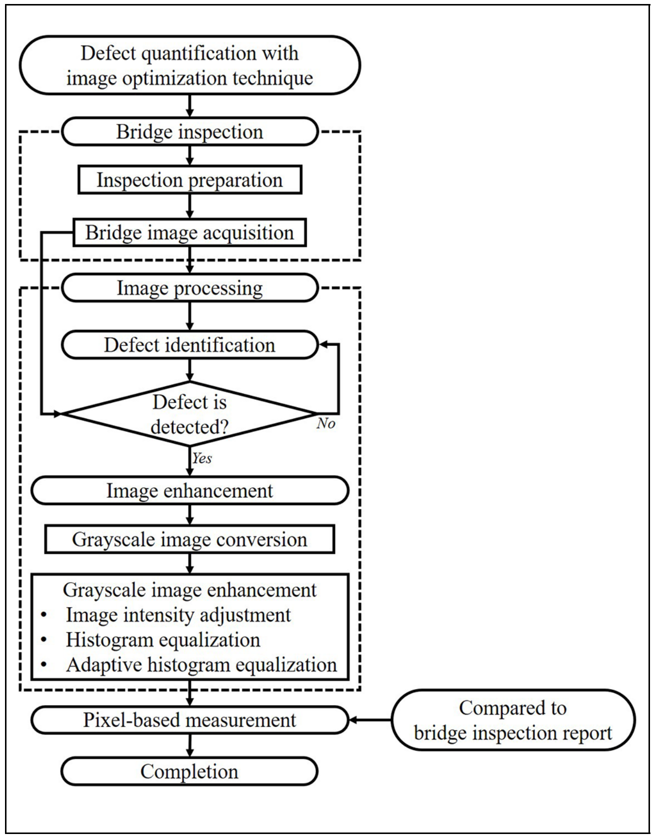

Figure 1. Framework for the defect quantification using enhanced image processing.

The second step comprises three sub-steps: defect identification, grayscale image enhancement, and defect quantification. In defect identification, inspectors can visually observe the bridges using the inspection images obtained from the drone. If deterioration on the bridge is detected, image enhancement and pixel-based measurement are performed using images extracted from the recorded videos. During the grayscale image enhancement, color images should be converted to the grayscale image to adjust the contrast of the image. After the image conversion, grayscale image enhancement techniques incorporating the image's histogram adjustment are performed. For this study, three different techniques including image intensity adjustment, histogram equalization, and adaptive histogram equalization are applied for image visibility enhancement. The image intensity adjustment technique saturates the contrast having values of 1% of top (contrast 255, white) and 1% of bottom (contrast 0, black) to other contrasts (*25*). An entire shape of histogram, excluding the top and bottom 1%, is similar to the histogram of the grayscale image. The histogram equalization technique involves transforming the intensity values so that the histogram of the output image in grayscale approximately matches the histogram distributed uniformly (*25*). By default, the histogram equalization technique attempts to match a flat histogram with 64 bins, but users can specify a different histogram instead. As an alternative to using the histogram equalization, the adaptive histogram equalization technique can be performed using contrast-limited adaptive histogram equalization (*25*). Whereas the histogram equalization can be applied on the entire image, the adaptive histogram equalization can be specifically useful on small regions in the image, called "tiles." The adaptive histogram equalization enhances the contrast of each tile so that the histogram of the output region approximately matches a specified histogram (*25*). After performing the equalization, adaptive histogram equalization combines neighboring tiles using bilinear interpolation to eliminate artificially induced boundaries.

With the visually enhanced images, the pixel-based measurement technique can be conducted to quantify the defect in the image. This technique can count the number of pixels to measure the length of the defect on the image. This measured length is a relative length and the identified length, reference length, is required to obtain an actual length of the defect. Dimensions of the bridge elements are commonly reference lengths for this measurement. As an example of the reference lengths, a girder width and depth of the deck can be used. With the ratio of the reference length and number of pixels for the reference length and the defect, the actual length of defect can be calculated. Through this process, the pixel numbers of reference and defect have an influence on the accuracy of the measurement results; thus, the visually enhanced images are required for high accuracy. To calibrate the accuracy of the measurement results through this framework, the results can be compared with the field measurements. It should be noted that the direct defect measurements can be performed using traditional inspection devices such as tapes during the inspection or relevant quantifiable data can be acquired from the bridge inspection reports published from State Departments of Transportation (DOTs).

Selected Bridge

A three-span bridge (see Figure 2) located in Keystone, South Dakota, was selected for the drone-enabled inspection performed on September 9, 2019. This bridge was constructed in 1968 and is part of a three-level interchange without a water crossing. This bridge consists of concrete decking and four glue-laminated timber girders. Bridge railings are installed along both sides of the concrete decking to increase safety of motorists. Metal diaphragms are installed between the girders at the underside of the bridge for increased lateral stability. Timber column piers and concrete abutments are used for the (simply supported) bridge superstructure. The average daily traffic of this bridge is 1,968 vehicles in accordance with National Bridge Inventory data (*26*). This bridge has a single lane for one-way traffic. Because of a relatively high volume of traffic specific to the one-way roadway, the drone-aided inspection was selected for this study rather than traditional inspection methods requiring UBIVs/UBITs.

Figure 2. Three-span timber girder bridge located in Keystone, South Dakota.

Description of Drone

A DJI Matrice 210 drone was chosen for image acquisition to efficiently inspect the bridge. The drone dimensions are 887 × 880 × 378 mm (L × W × H) and weight 4.57 kg. This drone can hover with 1.57 kg of supplemental equipment such as sensors. The maximum hovering speed and time are 18 m/s and 12 min, respectively. This drone can hover safely under 12 m/s and can be remotely controlled up to 7 km away from the remote controller. To acquire high-quality images, drone-mounted Zenmuse X5S (gimbal sensor), which has a complementary metal-oxide-semiconductor camera sensor with dimensions of 17.3 mm width × 13.0 mm height (4/3 in. type). This sensor has 20.8 megapixels and can record (MOVie formatted) videos with 4K digital cinema initiatives resolution (4,096 × 2,160 pixels).

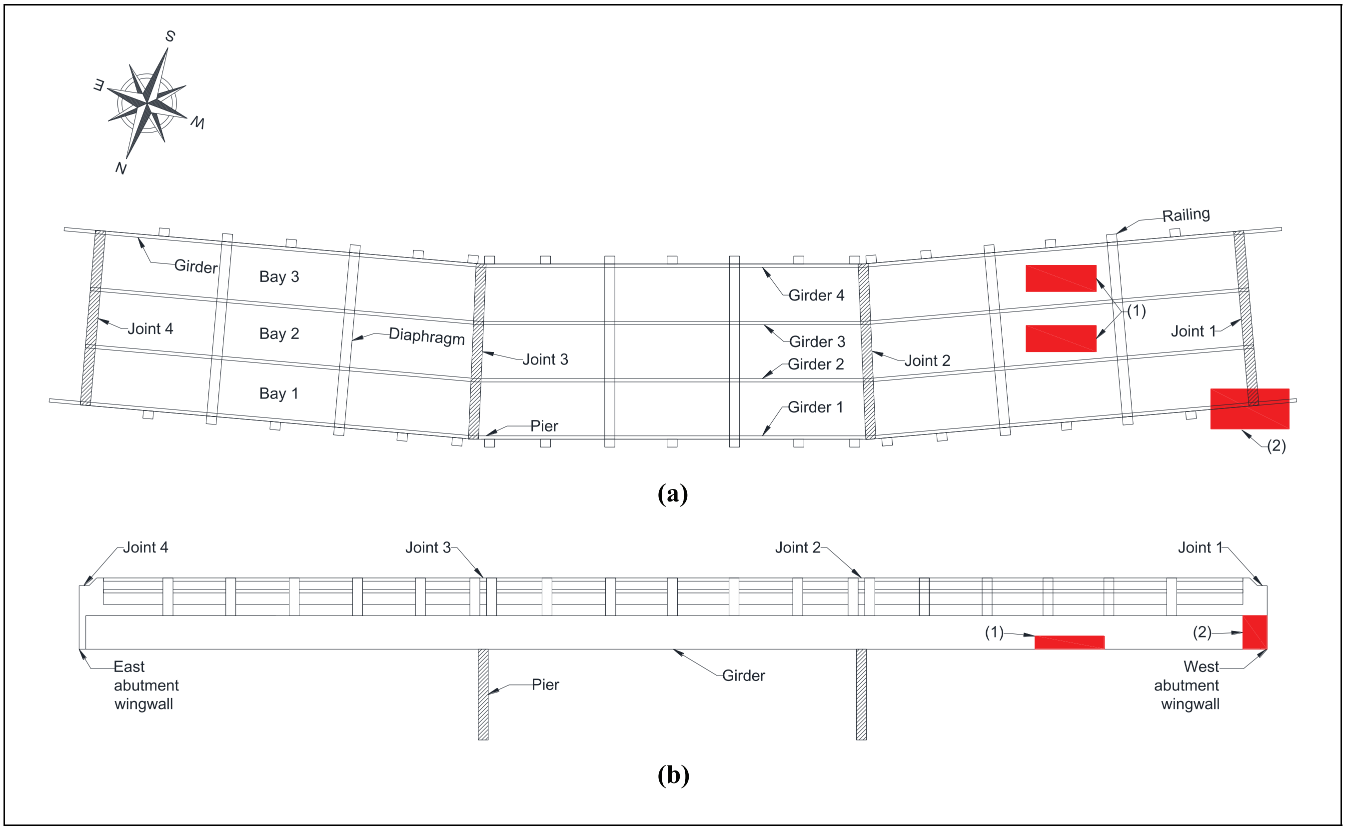

Figure 3. Sketch of three-span timber girder bridge with marked visible defect: (*a*) plan view and (*b*) elevation view.

Results and Discussion

With inspection images captured from the drone in field application, defect identification, image visibility improvement, and defect quantification were performed with representative defect such as water leakage. To improve image visibility, the proposed framework focusing on the grayscale enhancement techniques were applied to this study. With visually enhanced images, defect measurement was conducted using ImageJ, which measures the length of defect based on the pixel-based measurement technique. All the details for the bridge inspection through the defect quantification can be provided as follows.

Inspection and Image Collection

A sketch for the bridge at the beginning of the framework application was developed based on the inspection report as shown in Figure 3. Figure 3, *a* and *b*, show the plan view and elevations of the bridge, respectively. During defect identification, a representative defect on the bridge is marked with red rectangles as displayed in Figure 3, *a* and *b*. Two locations (1) and (2) are marked. Defect 1 indicates defects because of water leakage, discoloration, efflorescence, and spalling underneath the deck. Defect 2 includes spalling and water leakage on the abutment. For the safe drone-aided inspection underneath the deck, the remote controller operated the drone on its sport mode allowed for avoidance of any obstacles. The visual observer carefully monitored the drone in flight to inform the remote controller of any hazards or obstacles.

During the inspection, significant defects because of water leakage, crack, spalling, and efflorescence underneath the deck and discoloration on the timber girder (see Figure 4*a*) and spalling and water leakage on the abutment (see Figure 4*b*) were detected as shown in Figure 4. In Figure 4*a*, the area of spalling and discoloration and concrete cracks with built-up efflorescence are identified, but the boundaries of efflorescence and water leakage underneath the deck are not observed. These boundaries for efflorescence and water leakage were not used for the efficient defect quantification during image analysis using Figure 4*a* because of low brightness. On the other hand, the boundaries of deterioration because of spalling and crack were identified. In Figure 4*b*, the spalling and water leakage on the concrete abutment are identified, but the edge of each defect is still challenging to discover because of darkness of the inspection image.

The proposed grayscale image enhancement techniques integrated with a conversion tool available in

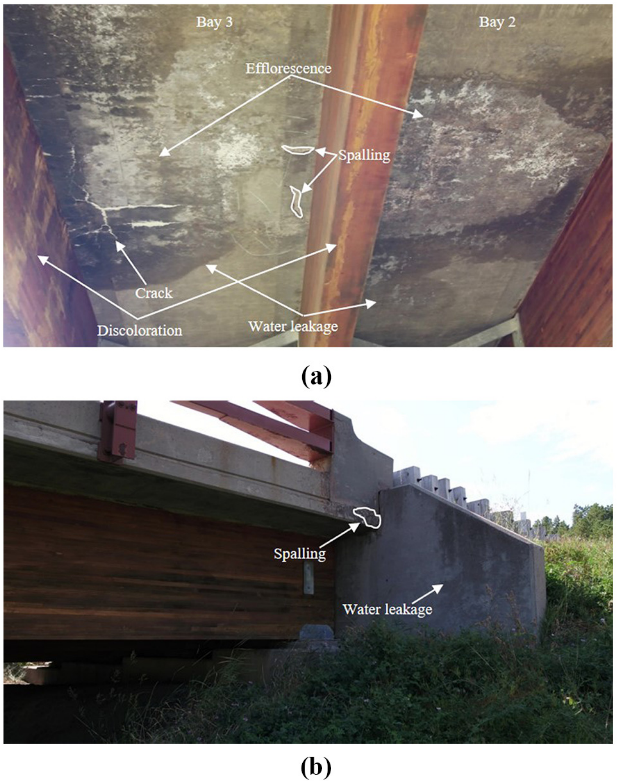

Figure 4. Representative defect images obtained by drone: (*a*) water leakage, discoloration, efflorescence, crack, and spalling underneath the deck; and (*b*) water leakage and spalling on the abutment wingwall.

MATLAB, enabling the conversion of unfiltered color images to grayscale images, was able to resolve the issue in Figure 4, *a* and *b*. Details on how to improve the quality of the images (Figure 4, *a* and *b*) are presented in the following sections.

Visual Inspection using Visually Enhanced Images

To improve the efficiency of visual inspection, the image enhancement techniques were applied to the inspection of images (Figure 4, *a* and *b*) having different types of visible defect as displayed in Figures 5 and 6. Comprehensively, these inspection images were converted to the grayscale image first as shown in Figures 5*a* and 6*a*. Following the grayscale conversion, the visibility of the grayscale images were enhanced using three different techniques: (a) image intensity adjustment (see Figures 5*c* and 6*c*), (b) histogram equalization (see Figures 5*e* and 6*e*), and (c) adaptive histogram equalization (see Figures 5*g* and 6*g*). Histograms were also provided next to each conversion and technology, as shown in Figures 5 and 6, to observe the numerical difference in each image. For instance, the histograms for the grayscale images are provided in Figures 5*b* and 6*b* and the histograms of images enhanced with image intensity adjustment technique can be seen in Figures 5*d* and 6*d*.

The relationship between the quality of image and the different techniques is examined by comparing the visibility of the images. In the grayscale image (see Figure 5*a*), the boundaries of deteriorations because of efflorescence and water leakage identified in Bays 2 and 3 are not observed clearly. As shown in Figure 5*b*, the contrasts (columns in Figure 5*b*) vary between 30 and 210 in this image. The visibility of the grayscale image is enhanced by the image intensity adjustment technique as shown in Figure 5*c*, indicating the areas of defects with slight improvement in contrast than in the grayscale image. The shapes of histograms shown in Figure 5, *b* and *d*, are observed to be similar. On the other hand, the areas of defects are not clearly observed after applying the histogram equalization technique as shown in Figure 5*e*. The boundaries of water leakage in Bay 3 are not identified in Figure 5*e*. Contrasts are degraded as displayed in Figure 5*e* as this technique utilizes only 64 bins (Figure 5*f*). The grayscale image enhanced with the adaptive histogram equalization technique shows significant improvement in visibility with clear boundaries of the defects because of water leakage and efflorescence as shown in Figure 5*g*. As shown in Figure 5*h*, the histogram of this technique shows uniform distribution of contrasts compared with the other techniques. The adaptive histogram equalization is considered the finest technique for the image enhancement for Figure 5*a*.

Figure 6 shows the applications of visibility enhancement technique for Figure 4*b*. Although the spalling and water leakage on the abutment wingwall are identified, the boundaries of the deteriorations are not observed distinctly in Figure 6*a* because of poor distribution of contrast (see Figure 6*b*). Figure 6*a* adjusted with the image intensity adjustment technique (Figure 6*c*) shows the similar image quality as that of Figure 6*a*, and the histogram of Figure 6*d* is also found to be analogous to Figure 6*b*. The boundaries of the defect area are also observed to be unclear as shown in Figure 6*c*. Compared with Figure 6, *a* and *c*, the grayscale image adjusted with the histogram equalization technique (Figure 6*e*) is observed to be significantly brighter as the ratio of the contrasts that are near to the white (contrast 255) are higher than in histograms of Figure 6, *b* and *d*. In Figure 6*e*, the area of water leakage on the abutment wingwall can be observed more noticeably than in Figure 6, *a* and *c*, but the boundaries of spalling cannot be detected obviously. The boundaries of defects because of spalling and water leakage are observed in the grayscale image adjusted with the adaptive histogram equalization as displayed in Figure 6*g*. The histogram of the image for this

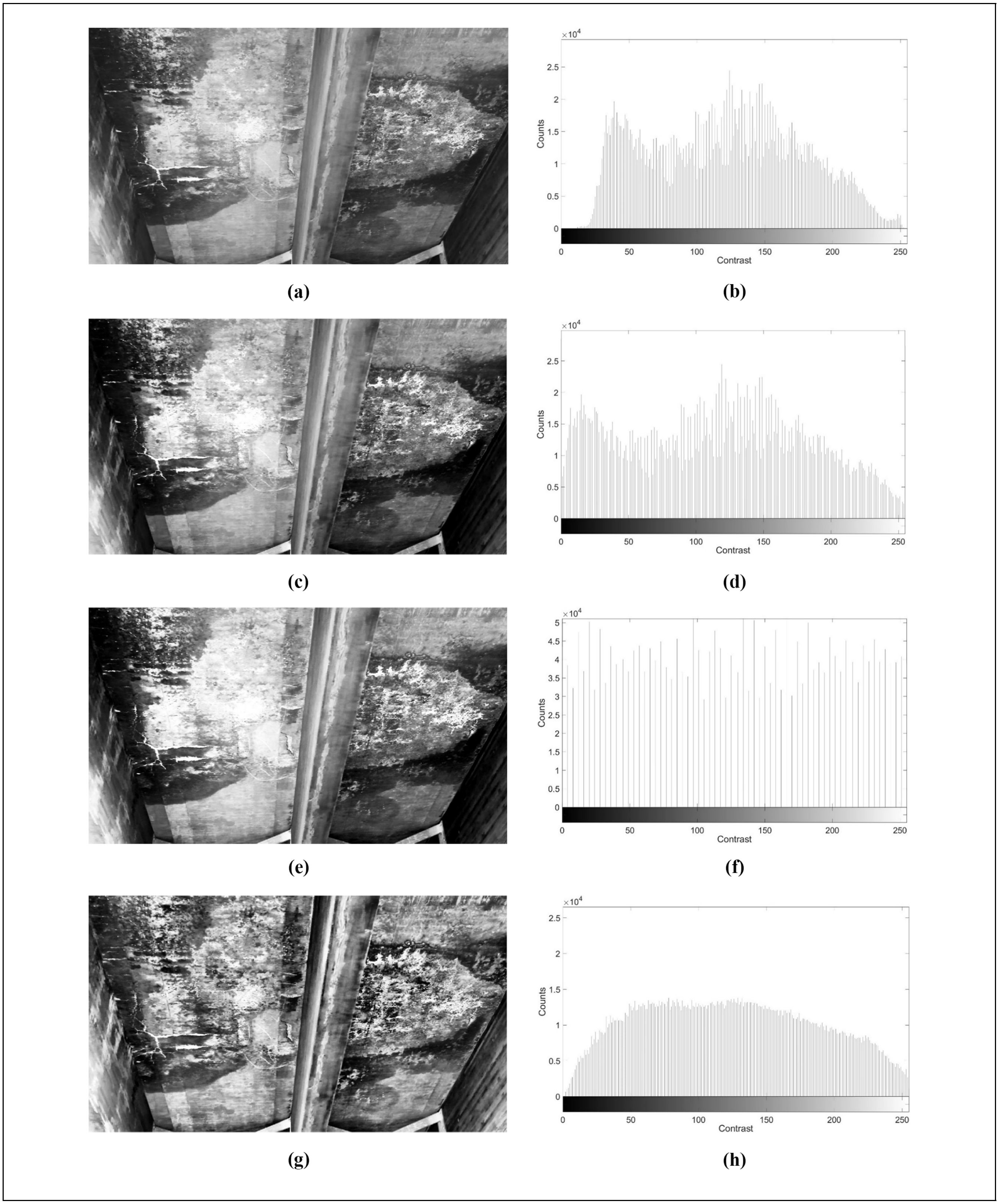

Figure 5. Grayscale image enhancement using drone-based color image shown in Figure 4*a*: (*a*) grayscale image conversion, (*b*) histogram of grayscale image application, (*c*) image intensity adjustment application, (*d*) histogram of image intensity adjustment application, (e) histogram equalization application, (*f*) histogram of histogram equalization application, (*g*) adaptive histogram application, and (*h*) histogram of adaptive histogram equalization application.

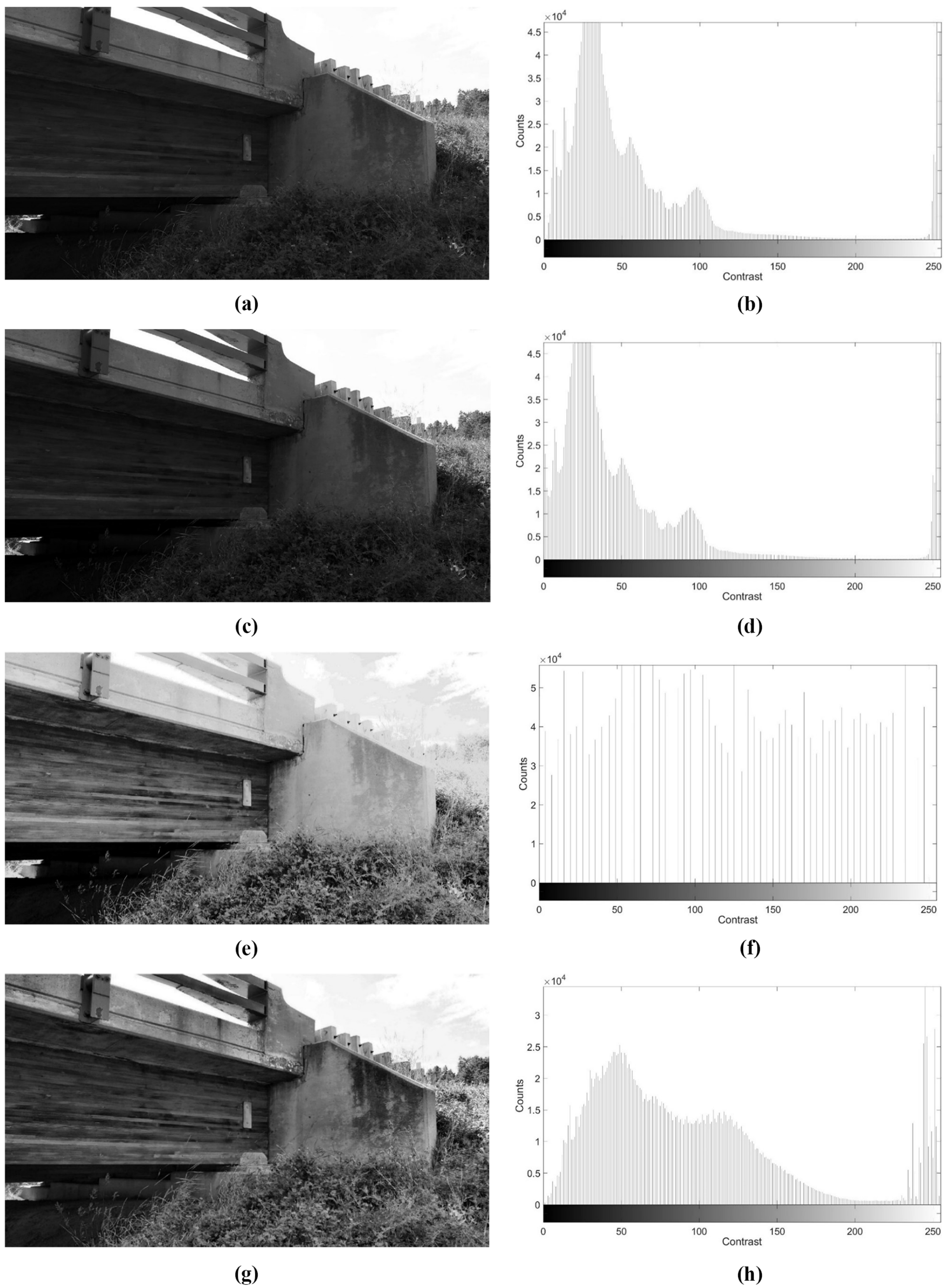

Figure 6. Grayscale image enhancement using drone-based color image shown in Figure 4*b*: (*a*) grayscale image conversion, (*b*) histogram of grayscale image application, (*c*) image intensity adjustment application, (*d*) histogram of image intensity adjustment application, (*e*) histogram equalization application, (*f*) histogram of histogram equalization application, (*g*) adaptive histogram application, and (*h*) histogram of adaptive histogram equalization application.

technique (see Figure 6*h*) shows uniform distribution of contrasts compared with the other histograms. From these results of the image enhancement technologies, the adaptive histogram equalization is found to be the most appropriate technique for investigating the defects.

Defect Measurement

Following the image enhancement techniques, spatial properties (i.e., area) of the visible defect inflicted on the bridge elements were quantified using ImageJ, which is the software to measure the length with the pixel-based technique. This software was able to measure the length of the defect using the number of pixels in the images. Note, it is required that the measured length be used directly for the defect quantification as the measured length is relative to each of the images. The actual length and the number of pixels of reference length that was determined based on the dimension of the bridge girder depth and width were employed from which the actual length of the defect can be calculated using the ratio between the defect and reference lengths. It should be noted that the direct measurements of the defect that can be used to calibrate the techniques were not able to be performed because the defects were located in inaccessible areas. According to the above defect measurement procedure, the identified defect underneath the deck (see Figure 5) and on the concrete abutment wingwall (see Figure 6) was measured. In Figure 5*g*, the areas of defects because of efflorescence, water leakage, discoloration, crack, and spalling were measured as shown in Figure 7. To detect the boundaries to each defect, a magnified grayscale image per defect was used to identify corresponding boundaries that were measured using ImageJ. With the enhanced grayscale images, the boundaries of deteriorations were more obviously observed compared with the use of the unfiltered image (refer to Figure 4), resulting in more accurate measurements. Following this procedure, the crack length and width, efflorescence, water leakage, spalling, and discoloration were measured along the identified orange lines, yellow dashed lines, blue lines, green lines, and purple lines, respectively, as marked in Figure 7. Specifically, in this figure, the defect in the image was marked with a red line and the length of the marked area was measured. With the same measurement processing, the areas of efflorescence, water leakage, crack, and spalling underneath the deck were measured to be 3.75 m^2, 4.21 m^2, 0.02 m^2, 0.74 m^2, respectively, whereas the area of discoloration on the timber girder was measured to be 2.12 m^2. In particular, the measured crack width and length were, on average, 12.58 mm and 1.59 m, respectively. According to the South Dakota DOT (SDDOT) bridge inspection reports (*27, 28*), the efflorescence observed and field measured to

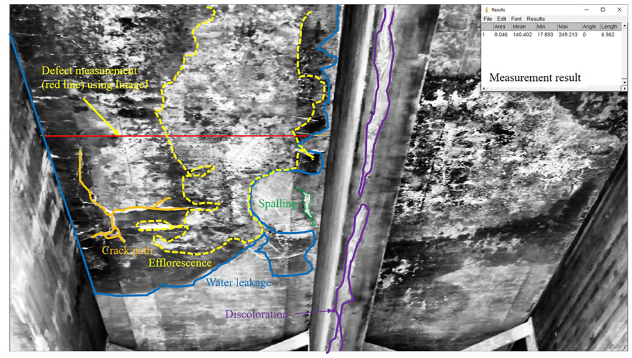

Figure 7. Measurement for the defect underneath the concrete deck.

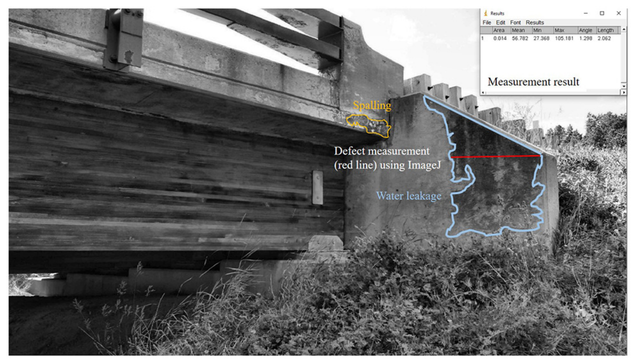

Figure 8. Measurement for the defect on the concrete abutment wingwall.

be approximately $0.76 \times 0.91\,m^2$ ($0.69\,m^2$) was reported but the field measurements for the other detects were not specifically presented in the report. The difference in the efflorescence acquired from the framework and inspection report can be attributed to the framework being able to clearly identify the boundaries to the efflorescence within the enhanced visualization of grayscale images.

Defects because of spalling and water leakage were also quantified as depicted in Figure 8, following the identical procedure as described above. For this measurement, the grayscale image with the adaptive histogram equalization technique (see Figure 6*g*) was used as the final input image. Using ImageJ, the area of water leakage (blue boundaries in Figure 8) on the concrete abutment wingwall was measured and spalling on the concrete deck (orange boundaries in Figure 8) were measured to be 1.63 m^2 and 0.26 m^2, individually on Figure 6*g*. The boundary detection and measurement were conducted following the same procedure as in the defect identification underneath the deck. According to the SDDOT inspection reports (*27, 28*), the size of spalling was field measured to be $0.61 \times 0.15\,m^2$ ($0.09\,m^2$), but the measured area of water leakage was not included in the reports. The difference in the size of spalling can be caused by precisely identifying the spalling boundaries across the enhanced grayscale image against the field measurement.

Conclusions

This study is aimed at performing defect identification and measurement with high-quality images obtained from the proposed grayscale enhancement techniques coupled with drone inspection images. To that end, the drone inspection was conducted on September 9, 2019 on an existing three-span timber girder bridge with concrete decking. The drone recorded the defects with video files, and all images necessary for image analysis were extracted from the video (MOV extension) to identify and measure the defects. By analyzing all the results, the following conclusions have been drawn:

1. From the bridge inspection, which collected drone images, a variety of defect types including water leakage, spalling, efflorescence, and discoloration were identified in the inspected bridge.
2. Grayscale image enhancement techniques improved image visibility and defect identification from the unfiltered inspection images along with improvement in visibility of the defect boundaries.
3. Pixel-based measurement coupled with grayscale image enhancement techniques was capable of accurately and efficiently measuring the size of the defects because of efflorescence, water leakage, and spalling underneath the concrete deck and discoloration on the girder.
4. Defects because of efflorescence, water leakage, crack, and spalling underneath the concrete deck and discoloration on the girder were identified and their areas were measured to be $3.75\,m^2$ (efflorescence), $4.21\,m^2$ (water leakage), $0.02\,m^2$ (crack), $0.74\,m^2$ (spalling), and $2.12\,m^2$ (discoloration), individually.
5. On the concrete abutment wingwall, the water leakage and spalling were measured to be $1.63\,m^2$ and $0.26\,m^2$, respectively, using the image adjusted with the adaptive histogram equalization application.
6. The efflorescence and spalling quantified via the proposed techniques were particularly compared with the field measurements included in the SDDOT inspection reports (*27, 28*). The difference in the defects measured from the techniques and inspection reports was found, and it can be explained by the techniques enabling the use of the grayscale images to identify the boundaries of each of the defects accurately.

As future work, a tool to automatically identify and measure the defect boundaries through the proposed techniques is needed. It is also necessary to perform multiple comparison testing with the direct measurements to validate the proposed techniques.

Acknowledgment

The assistance and cooperation of the South Dakota Department of Transportation engineers is gratefully acknowledged.

Author Contributions

The authors confirm contribution to the paper as follows: study conception and design: J. Seo, J. Wacker; data collection: J. Seo, E. Jeong; analysis and interpretation of results: E. Jeong, J. Seo, J. Wacker; draft manuscript preparation: E. Jeong, J. Seo, J. Wacker. All authors reviewed the results and approved the final version of the manuscript.

Declaration of Conflicting Interests

The author(s) declared no potential conflicts of interest with respect to the research, authorship, and/or publication of this article.

Funding

The author(s) disclosed receipt of the following financial support for the research, authorship, and/or publication of this article: Partial financial support for this research was provided by the United States Department of Agriculture (USDA), Forest Service through Joint Venture Agreement No. 18-JV-11111133-031 and in conjunction with the Forest Products Laboratory (FPL).

Data Accessibility Statement

The data collected from the bridge inspections that support the findings of this study are available from the corresponding author on reasonable request.

References

1. Bennett, M. The High-Flying Job That's Not for the Faint-Hearted. *BBC News*, 2019.
2. Cunningham, K., D. Lattanzi, R. Dell'Andrea, M. Riley, T. Huette, R. Goetz, and R. Wilson. UAS-Based Inspection of the Placer River Trail Bridge: A Data-Driven Approach. *Proc., Structures Congress 2015*, Portland, OR, 2015, pp. 607–615.
3. Duque, L., J. Seo, and J. P. Wacker. Timber Bridge Inspection using UAV. In *Proc., Bridges, Transportation Structures, and Nonbuilding Structures: Structures Congress*

2018 (J. G. Soules, ed.), Fort Worth, TX, April 19–21, 2018, American Society of Civil Engineers, Reston, VA, Pp. 186–196.
4. Duque, L., J. Seo, and J. P. Wacker. Synthesis of Unmanned Aerial Vehicle Applications for Infrastructures. *Journal of Performance of Constructed Facilities*, Vol. 32, No. 4, 2018, p. 04018046. https://doi.org/10.1061/(ASCE)CF.1943-5509.0001185.
5. Hallermann, N., and G. Morgenthal. Visual Inspection Strategies for Large Bridges using Unmanned Aerial Vehicles (UAV). *Proc., International Conference on Bridge Maintenance, Safety and Management*, Shanghai, 2014, pp. 661–667.
6. Jeong, E., J. Seo, and J. P. Wacker. Literature Review and Technical Survey on Bridge Inspection using Unmanned Aerial Vehicle. *Journal of Performance of Constructed Facilities*, Vol. 34, No. 6, 2020, p. 04020113. https://doi.org/10.1061/(ASCE)CF.1943-5509.0001519.
7. Jeong, E., J. Seo, and J. P. Wacker. New Bridge Inspection Approach with Joint UAV and DIC System. *Proc., ASCE Structures Congress 2020*, St. Louis, MO, 2020.
8. Khaloo, A., D. Lattanzi, K. Cunningham, R. Dell'Andrea, and M. Riley. Unmanned Aerial Vehicle Inspection of the Placer River Trail Bridge through Image-Based 3D Modelling. *Structure and Infrastructure Engineering*, Vol. 14, No. 1, 2018, pp. 124–136. https://doi.org/10.1080/15732479.2017.1330891.
9. Otero, L. D., N. Gagliardo, D. Dalli, W.-H. Huang, and P. Cosentino. *Proof of Concept for using Unmanned Aerial Vehicles for High Mast Pole and Bridge Inspections*. Publication BDV28 TWO 977-02. Florida Department of Transportation, Melbourne, 2015, p. 170.
10. Seo, J., L. Duque, and J. P. Wacker. Drone-Enabled Bridge Inspection Methodology and Application. *Automation in Construction*, Vol. 94, 2018, pp. 112–126. https://doi.org/10.1016/j.autcon.2018.06.006.
11. Seo, J., J. P. Wacker, and L. Duque. *Evaluating the Use of Drones for Timber Bridge Inspection*. Publication General Technical Report FPLGTR-258. U.S. Department of Agriculture, Forest Service, Forest Products Laboratory, Madison, WI, 2018, p. 145.
12. Seo, J., L. Duque, and J. P. Wacker. Field Application of UAS-Based Bridge Inspection. *Transportation Research Record: Journal of the Transportation Research Board*, 2018. 2672: 72–81.
13. Seo, J., L. Duque, and J. P. Wacker. Glued-Laminated Timber Arch Bridge Inspection Using UAV. In *Proc., Smart Cities, Sustainability, and Resilience: Computing in Civil Engineering 2019* (Y. K. Cho, F. Leite, A. Behzadan, and C. Wang, eds.), Atlanta, Georgia, June 17–19, 2019, American Society of Civil Engineers, Reston, VA, pp. 336–342.
14. Zink, J., and B. Lovelace. *Unmanned Aerial Vehicle Bridge Inspection Demonstration Project*. Publication MN/RC 2015-40. Minnesota Department of Transportation, Oakdale, 2015, p. 214.
15. Duque, L., J. Seo, and J. P. Wacker. Bridge Deterioration Quantification Protocol using UAV. *Journal of Bridge Engineering*, Vol. 23, No. 10, 2018, p. 04018080. https://doi.org/10.1061/(ASCE)BE.1943-5592.0001289.
16. Dervilis, N., M. Choi, S. G. Taylor, R. J. Barthorpe, G. Park, C. R. Farrar, and K. Worden. On Damage Diagnosis for a Wind Turbine Blade using Pattern Recognition. *Journal of Sound and Vibration*, Vol. 333, No. 6, 2014, pp. 1833–1850. https://doi.org/10.1016/j.jsv.2013.11.015.
17. Jahanshahi, M. R., S. F. Masri, C. W. Padgett, and G. S. Sukhatme. An Innovative Methodology for Detection and Quantification of Cracks through Incorporation of Depth Perception. *Machine Vision and Applications*, Vol. 24, No. 2, 2013, pp. 227–241. https://doi.org/10.1007/s00138-011-0394-0.
18. Kelm, B. M., B. H. Menze, C. M. Zechmann, K. T. Baudendistel, and F. A. Hamprecht. Automated Estimation of Tumor Probability in Prostate Magnetic Resonance Spectroscopic Imaging: Pattern Recognition vs Quantification. *Magnetic Resonance in Medicine*, Vol. 57, No. 1, 2007, pp. 150–159. https://doi.org/10.1002/mrm.21112.
19. Reagan, D. *Unmanned Aerial Vehicle Measurement using Three - Dimensional Digital Image Correlation to Perform Bridge Structural Health Monitoring*. University of Massachusetts Lowell, Ann Arbor, MI, 2014.
20. Reagan, D., A. Sabato, and C. Niezrecki. Unmanned Aerial Vehicle Acquisition of Three-Dimensional Digital Image Correlation Measurements for Structural Health Monitoring of Bridges. *Proc., SPIE Smart Structures and Materials + Nondestructive Evaluation and Health Monitoring*, Portland, OR, 2017.
21. Reagan, D., A. Sabato, and C. Niezrecki. Feasibility of using Digital Image Correlation for Unmanned Aerial Vehicle Structural Health Monitoring of Bridges. *Structural Health Monitoring*, Vol. 17, No. 5, 2017, pp. 1056–1072. https://doi.org/10.1177/1475921717735326.
22. Maini, R., and H. Aggarwal. A Comprehensive Review of Image Enhancement Techniques. *arXiv Preprint arXiv:1003.4053*, 2010.
23. Russ, J. C. *The Image Processing Handbook*. CRC Press, Boca Raton, FL, 1992.
24. Federal Aviation Administration (FAA). Getting Started. https://www.faa.gov/uas/getting_started/. Accessed September 27, 2020.
25. MATLAB & Simulink. Enhance Grayscale Images. https://www.mathworks.com/help/images/contrast-enhancement-techniques.html. Accessed July 24, 2020.
26. Federal Highway Administration (FHWA). National Bridge Inventory (NBI) Data. US Department of Transportation, FHWA, Washington, D.C., 2020.
27. Sauter, N., and S. Kamarainen. *Bridge Inspection Report for Structure Number 52-308-411*. South Dakota Department of Transportation (SDDOT), Pierre, 2016, p. 12.
28. Carson, T., and M. Leonard. *Bridge Inspection Report for Structure Number 52-308-411*. Stantec Consulting Services Inc., Edmonton, AB, 2018, p. 34.